Wave functions of $(I, J^P) = (\frac{1}{2}, \frac{3}{2}^{\mp})$ baryons

Langtian Liu (刘浪天)[1,2] Chen Chen (陈晨)[3,4,*] and Craig D. Roberts[1,2,†]

[1]*School of Physics, Nanjing University, Nanjing, Jiangsu 210093, China*
[2]*Institute for Nonperturbative Physics, Nanjing University, Nanjing, Jiangsu 210093, China*
[3]*Interdisciplinary Center for Theoretical Study, University of Science and Technology of China, Hefei, Anhui 230026, China*
[4]*Peng Huanwu Center for Fundamental Theory, Hefei, Anhui 230026, China*

Using a Poincaré-covariant quark + diquark Faddeev equation, we provide structural information on the four lightest $(I, J^P) = (\frac{1}{2}, \frac{3}{2}^{\mp})$ baryon multiplets. These systems may contain five distinct types of diquarks; but in order to obtain reliable results, it is sufficient to retain only isoscalar-scalar and isovector-axialvector correlations, with the latter being especially important. Viewed with low resolution, the Faddeev equation description of these states bears some resemblance to the associated quark model pictures; namely, they form a set of states related via orbital angular momentum excitation: the negative parity states are primarily P-wave in character, whereas the positive parity states are D wave. However, a closer look reveals far greater structural complexity than is typical of quark model descriptions, with P, D, S, F waves and interferences between them all playing a large role in forming observables. Large momentum transfer resonance electroexcitation measurements can be used to test these predictions and may thereby provide insights into the nature of emergent hadron mass.

I. INTRODUCTION

In working to understand the emergence of baryon mass and structure from quantum chromodynamics (QCD), it is crucial to employ a framework that ensures Poincaré invariance of observables [1] and natural to study color-singlet three-quark six-point Schwinger functions [2–4]. Baryons appear as poles in such Schwinger functions: the pole location reveals the mass (and width) of a given baryon; and the pole residue is that baryon's Poincaré-covariant bound-state wave function. The nucleon and its excited states appear in the isospin $I = \frac{1}{2}$ channel. Focusing on the proton because it is Nature's only stable hadron, then the lowest-mass spectral feature that can be associated with the $(I, I_z) = (\frac{1}{2}, +\frac{1}{2})$ six-point Schwinger function is an isolated pole on the real axis. Owing to confinement [5–7], there is no three-quark continuum; but the related spectral functions exhibit additional structures associated with proton resonances that are attached to poles in the complex plane [8–11].

Working with the appropriate Schwinger function and using standard techniques, one can derive a Poincaré-covariant Faddeev-like equation whose solution provides the masses and wave functions of all baryons with the Poincaré-invariant quantum numbers that characterise the channel under consideration. For instance, the proton and all its radial excitations appear as positive parity solutions of a Faddeev equation derived from the $J = \frac{1}{2}$ Schwinger function. The parity partners of these states arise as the negative parity solutions. Today it is possible to develop a tractable formulation of such problems using the leading-order (rainbow-ladder, RL) truncation in a systematic scheme developed for the continuum bound-state problem [12–15]. The resulting equations have been solved for many baryons [16–21]. Although RL truncation does not produce widths for the states, sensible interpretations of the results are available [22–24], *viz.* the solutions are understood to represent the dressed-quark core of the considered baryon, which is subsequently dressed via meson-baryon final-state interactions [25–29].

An alternative approach to the Poincaré-covariant Faddeev equation exploits the fact that any interaction which provides a good description of ground-state color-singlet mesons also generates strong color-antitriplet correlations between any two dressed quarks contained within a hadron [11]. This understanding leads to the quark–plus–dynamical-diquark picture of baryon structure, formulated elsewhere [30–33] and illustrated in Fig. 1. Here, the kernel
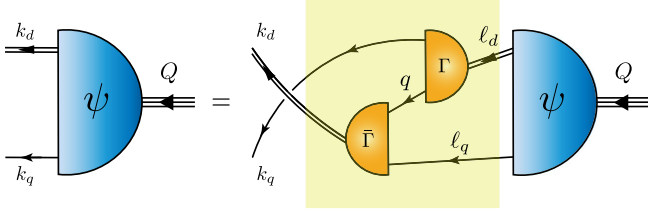
---

*chenchen1031@ustc.edu.cn
†cdroberts@nju.edu.cn

FIG. 1. Quark + diquark Faddeev equation, a linear integral equation for the Poincaré-covariant matrix-valued function ψ, the Faddeev amplitude for a baryon with total momentum $Q = \ell_q + \ell_d = k_q + k_d$. ψ describes the relative momentum correlation between the dressed-quarks and -diquarks. Legend. Shaded rectangle: Faddeev kernel; single line: dressed-quark propagator, $S(q = \ell_d - k_q)$; $\Gamma^{d}(k; K)$: diquark (d) correlation amplitude; and double line: diquark propagator, $\Delta^{d}(K)$.

is built using dressed-quark and nonpointlike diquark degrees-of-freedom, with binding energy stored within the diquark correlation and additionally generated by the exchange of a dressed-quark, which emerges as one diquark breaks up and is absorbed into formation of another. In general, many diquark correlations are possible: isoscalar-scalar, $(I, J^P = 0, 0^+)$; isovector-axialvector; isoscalar-pseudoscalar; isoscalar-vector; and isovector-vector. Within a given system, channel dynamics determines the relative strengths of these correlations.

The Faddeev equation in Fig. 1 has been used to study the structure of the proton and its lightest $J^P = \frac{1}{2}^{\pm}$ excitations [34]. The results indicate that scalar and axialvector diquarks are dominant in the proton and Roper resonance; the associated rest-frame wave functions are primarily S-wave in character; and the Roper resonance is, at heart, the proton's lightest radial excitation [35–37]. The predicted presence of axialvector diquarks within the nucleon has far-reaching implications for, *inter alia*, form factors and structure functions [38–44].

Regarding $J^P = \frac{1}{2}^{-}$ states, accurate estimates of their masses are obtained by keeping only axialvector diquarks; odd-parity diquarks appear with material strength in the bound-state amplitudes, affecting electroproduction form factors [45]; the rest-frame wave functions are dominated by P-waves, but contain noticeable S-wave components; and the first excited state, $N(1650)\frac{1}{2}^{-}$, has little of the appearance of a radial excitation of the $N(1535)\frac{1}{2}^{-}$.

So long as rest-frame orbital angular momentum is identified with that existing between dressed-quarks and -diquarks, there are some similarities here with quark model descriptions of $J^P = \frac{1}{2}^{\pm}$ systems. Notwithstanding that, it should be stressed that in contrast to quark model expectations [46], the negative parity states are not simply angular-momentum excitations of the $J^P = \frac{1}{2}^{+}$ ground-states. It is worth highlighting here that, *inter alia*, any separation of a system's total angular momentum into a sum of constituent orbital angular momentum and spin, $J = L + S$, is frame dependent; hence, in quantum field theory, there is no direct

connection between parity—a Poincaré invariant quantity—and orbital angular momentum.

The Fig. 1 Faddeev equation approach was adapted to the analogous low-lying Δ-baryons in Ref. [47], revealing that although these states may contain isovector-axialvector and isovector-vector diquarks, the latter contribute little. The $J^P = \frac{3}{2}^{+}$ systems are the simpler, with some features being similar to quark model pictures, e.g., their dominant rest-frame orbital angular momentum component is S-wave and the $\Delta(1600)\frac{3}{2}^{+}$ looks much like a radial excitation of the $\Delta(1232)\frac{3}{2}^{+}$. The $J^P = \frac{3}{2}^{-}$ states are more complicated. In fact, the $\Delta(1940)\frac{3}{2}^{-}$ expresses little of the character of a radial excitation of the $\Delta(1700)\frac{3}{2}^{-}$; and although the rest-frame wave function of the latter is largely P-wave, matching quark model expectations, this is not true of the $\Delta(1940)\frac{3}{2}^{-}$, whose rest-frame wave function is mostly S-wave.

An entirely new landscape opens to view when one considers $(I, J^P) = (\frac{1}{2}, \frac{3}{2}^{\mp})$ baryons. Drawn using the quark model, employing standard notation for SU(6) assignments, these states are interpreted as follows ([48], Sec. 15):

(i) $N(1520)\frac{3}{2}^{-}$ … $(70, 1_1^-)$, with constituent-quark orbital angular momentum being $L = 1$ and the sum of the three constituent-quark spins being $S = \frac{1}{2}$;

(ii) $N(1700)\frac{3}{2}^{-}$ … $(70, 1_1^-)$, $L = 1$, $S = \frac{3}{2}$;

(iii) $N(1720)\frac{3}{2}^{+}$ … $(56, 2_2^+)$, $L = 2$, $S = \frac{1}{2}$;

(iv) $N(1900)\frac{3}{2}^{+}$ … $(70, 2_2^+)$, $L = 2$, $S = \frac{3}{2}$;

One sees the parity-partner relationships (i), (iii) and (ii), (iv); but no state is related to another as radial excitation. Different structural pictures can emerge, e.g., in relativistic potential models [49,50] and light-front holographic descriptions of hadrons [51].

In quantum field theory, parity partners are special because all differences between them can be attributed to chiral symmetry breaking; and in the light-quark sector, such symmetry breaking is almost entirely dynamical. Dynamical chiral symmetry breaking is a corollary of emergent hadron mass (EHM) [52–58]; so, linked with confinement in ways that are not yet fully elucidated. Consequently, experiments that can test predictions made for structural differences between parity partners in the hadron spectrum are valuable [59–61]. Herein, therefore, we present the first predictions for the structure of low-lying $(\frac{1}{2}, \frac{3}{2}^{\mp})$ baryons based on the Poincaré-covariant Faddeev equation in Fig. 1, the interpretation and validation of which have the potential to shed new light on expressions of EHM in hadron observables.

Our treatment of $(\frac{1}{2}, \frac{3}{2}^{\mp})$-baryon bound-state problems is outlined in Sec. II. This sketch is sufficient because details are provided elsewhere, e.g., Refs. [24,34,47,62]. Section III reports predictions for the masses and diquark content of $(\frac{1}{2}, \frac{3}{2}^{\mp})$ baryons. A detailed picture of $(\frac{1}{2}, \frac{3}{2}^{\mp})$ wave functions and interrelationships is drawn in Sec. IV,

with particular attention paid to a rest-frame decomposition of their orbital angular momentum. Section V presents a summary and perspective.

II. BOUND STATE EQUATIONS

In solving for the masses and structure of $(\frac{1}{2}, \frac{3}{2}^{\mp})$ baryons, we aim for unification with existing analyses of $(\frac{1}{2}, \frac{1}{2}^{\pm})$, $(\frac{3}{2}, \frac{3}{2}^{\mp})$ states [34,47]. Hence, insofar as possible, the formulations therein are preserved, e.g.: we assume isospin symmetry throughout; the diquark correlation amplitudes, Γ^d, are similar; the light-quark and diquark propagators, S, Δ^d, are unchanged—see Ref. [47] (Appendix); and the effective masses of the relevant diquark correlations are (in GeV)

$$\begin{array}{cccc} m_{[ud]_{0^+}} & m_{\{uu\}_{1^+}} & m_{[ud]_{0^-}} & m_{[ud]_{1^-}} \\ 0.8 & 0.9 & 1.3 & 1.4 \end{array} \tag{1}$$

The mass splitting between diquarks of opposite parity is commensurate with that in the ρ-a_1 complex [48]. Moreover, following Ref. [47], we emulate Ref. [63] (Sec. 4.1.4) in electing not to include the $g_{\rm DB}$ channel-coupling suppression-factor discussed in Ref. [34] (Sec. II. E) because, as will become apparent, negative parity diquarks play a minor role in $(\frac{1}{2}, \frac{3}{2}^{\mp})$ baryons. Finally, we omit isovector-vector diquark correlations because, calculated as explained elsewhere [[34] Sec. II C], using the masses in Eq. (1), their coupling into all systems is negligible, e.g., it is just 24% of the isoscalar-vector strength and 1% of that associated with the isoscalar-scalar correlation.

For $(\frac{1}{2}, \frac{3}{2}^P)$ baryons represented as quark + diquark bound states, the full Faddeev amplitude has the form

$$\underline{\psi} = \psi_1 + \psi_2 + \psi_3, \tag{2}$$

where the subscript identifies that quark which is not participating in a diquark correlation and $\psi_{1,2}$ are obtained from $\psi_3 =: \psi$ by a cyclic permutation of all quark labels [30]. Now explicating Fig. 1, using a compact notation, the Faddeev equation takes the following form:

$$\psi^d_{(\mu)\rho}(k; Q)$$
$$= \int \frac{d^4\ell}{(2\pi)^4} \sum_{d'} K^{d,d'}_{(\mu\nu)}(k, \ell; Q) \psi^{d'}_{(\nu)\rho}(\ell; Q), \tag{3}$$

where $Q = (k_1 + k_2) + k_3 = k_d + k_q$ is the total momentum of the baryon, $Q^2 = \hat{Q}^2 M^2 = -M^2$, M is the baryon's mass; $k = (-k_d + 2k_3)/3$; d runs over the five types of diquark correlations described above; $\psi^d_{(\mu)\rho}(k; Q)$ are the associated components of the amplitude (the indices μ, ν are only present for pseudovector and vector diquarks); and

the index ρ expresses the Rarita-Schwinger character of the solution.

The kernel in Eq. (3) realizes the processes in the shaded part of Fig. 1, *viz.* diquark breakup, quark propagation, and diquark reformation. It forges links between all diquark correlations in the complete amplitude and has the following structure:

$$K^{d,d'}_{(\mu\nu)}(k, \ell; Q) = \Gamma^{d'}_{(\alpha)}(k_q - \ell_d/2; \ell_d)$$
$$\times S^{\rm T}(q) \bar{\Gamma}^d_{(\mu)}(\ell_q - k_d/2; -k_d) S(\ell_q) \Delta^{d'}_{\alpha\nu}(\ell_d), \tag{4}$$

where $k_q = k + Q/3$, $\ell_q = \ell + Q/3$, $\ell_d = -\ell_q + Q$; and "T" denotes matrix transpose.

Expanding further and becoming more specific, focusing on the positive charge state of a given $(\frac{1}{2}, \frac{3}{2}^P)$ baryon, without loss of generality, the left-hand side of Eq. (3) is

$$\psi^P(k_i, \alpha_i, \sigma_i) = [\Gamma^{0^+}(\bar{k}; k_d)]^{\alpha_1\alpha_2}_{\sigma_1\sigma_2} \Delta^{0^+}(k_d) [\mathcal{S}^P_\rho(k; Q) u_\rho(Q)]^{\alpha_3}_{\sigma_3}$$
$$+ [t^j \Gamma^{1^+}_\mu] \Delta^{1^+}_{\mu\nu} [\mathcal{A}^{jP}_{\nu\rho}(k; Q) u_\rho(Q)]$$
$$+ [\Gamma^{0^-}] \Delta^{0^-} [\mathcal{P}^P_\rho(k; Q) u_\rho(Q)]$$
$$+ [\Gamma^{1^-}_\mu] \Delta^{1^-}_{\mu\nu} [\mathcal{V}^P_{\nu\rho}(k; Q) u_\rho(Q)], \tag{5}$$

where $(k_i, \sigma_i, \alpha_i)$ are the momentum, spin and isospin labels of the quarks constituting the bound state; $\bar{k} = (k_1 - k_2)/2$; t^j, $j = \{+, 0\}$, are axialvector diquark isospin matrices, with j summed in Eq. (5); and $u_\rho(Q)$ is a Rarita-Schwinger spinor, in which we have here suppressed the spin-projection label.

The matrix-valued functions that are contracted with the Rarita-Schwinger spinor in Eq. (5) can be expanded as follows:

$$\mathcal{S}^P_\rho(k; Q) = \sum_{i=1}^{2} v^i_{0^+}(k; Q) \mathcal{G}^P \mathcal{X}^i_\rho(k; Q), \tag{6a}$$

$$\mathcal{A}^{jP}_{\nu\rho}(k; Q) = \sum_{i=1}^{8} v^{ji}_{1^+}(k; Q) \mathcal{G}^P \mathcal{Y}^i_{\nu\rho}(k; Q), \tag{6b}$$

$$\mathcal{P}^P_\rho(k; Q) = \sum_{i=1}^{2} v^i_{0^-}(k; Q) \mathcal{G}^{-P} \mathcal{X}^i_\rho(k; Q), \tag{6c}$$

$$\mathcal{V}^P_{\nu\rho}(k; Q) = \sum_{i=1}^{8} v^i_{1^-}(k; Q) \mathcal{G}^{-P} \mathcal{Y}^i_{\nu\rho}(k; Q), \tag{6d}$$

where $\{v^{(j)i}_{J^P}(k; Q)\}$ are scalar functions, $\mathcal{G}^{+(-)} = \mathbb{I}_{\rm D}(i\gamma_5)$ and, with $T_{\mu\nu} = \delta_{\mu\nu} + \hat{Q}_\mu \hat{Q}_\nu$, $\gamma^\perp_\mu = T_{\mu\nu}\gamma_\nu$, $k^\perp_\mu = T_{\mu\nu}k_\nu$, $\hat{k}^\perp_\mu \hat{k}^\perp_\mu = 1$, the Dirac-matrix basis is

$$\mathcal{X}_\rho^1(k;Q) = i\sqrt{3}\hat{k}_\rho^\perp\gamma_5, \tag{7a}$$

$$\mathcal{X}_\rho^2(k;Q) = i\gamma\cdot\hat{k}^\perp\mathcal{X}_\rho^1(k;Q), \tag{7b}$$

$$\mathcal{Y}_{\nu\rho}^1(k;Q) = \delta_{\nu\rho}\mathbb{I}_D, \tag{7c}$$

$$\mathcal{Y}_{\nu\rho}^2(k;Q) = \frac{i}{\sqrt{5}}[2\gamma_\nu^\perp\hat{k}_\rho^\perp - 3\delta_{\nu\rho}\gamma\cdot\hat{k}^\perp], \tag{7d}$$

$$\mathcal{Y}_{\nu\rho}^3(k;Q) = -i\gamma_\nu^\perp\hat{k}_\rho^\perp, \tag{7e}$$

$$\mathcal{Y}_{\nu\rho}^4(k;Q) = \sqrt{3}\hat{Q}_\nu\hat{k}_\rho^\perp, \tag{7f}$$

$$\mathcal{Y}_{\nu\rho}^5(k;Q) = 3\hat{k}_\nu^\perp\hat{k}_\rho^\perp - \delta_{\nu\rho} - \gamma_\nu^\perp\hat{k}_\rho^\perp\gamma\cdot\hat{k}^\perp, \tag{7g}$$

$$\mathcal{Y}_{\nu\rho}^6(k;Q) = \gamma_\nu^\perp\hat{k}_\rho^\perp\gamma\cdot\hat{k}^\perp, \tag{7h}$$

$$\mathcal{Y}_{\nu\rho}^7(k;Q) = -i\gamma\cdot\hat{k}^\perp\mathcal{Y}_{\nu\rho}^4(k;Q), \tag{7i}$$

$$\mathcal{Y}_{\nu\rho}^8(k;Q) = \frac{i}{\sqrt{5}}[\delta_{\nu\rho}\gamma\cdot\hat{k}^\perp + \gamma_\nu^\perp\hat{k}_\rho^\perp - 5\hat{k}_\nu^\perp\hat{k}_\rho^\perp\gamma\cdot\hat{k}^\perp]. \tag{7j}$$

Moreover, with $\Lambda_+(Q) = (M - i\gamma\cdot Q)/(2M)$,

$$\frac{1}{2M}\sum_{r=-3/2}^{3/2} u_\rho(Q;r)\bar{u}_\mu(Q;r) = \Lambda_+(Q)R_{\rho\mu}, \tag{8a}$$

$$R_{\rho\mu} = \delta_{\rho\mu}\mathbb{I}_D - \frac{1}{3}\gamma_\rho\gamma_\mu + \frac{2}{3}\hat{Q}_\rho\hat{Q}_\mu\mathbb{I}_D - \frac{i}{3}[\hat{Q}_\rho\gamma_\mu - \hat{Q}_\mu\gamma_\rho]. \tag{8b}$$

Details of our Euclidean metric conventions are presented elsewhere ([64], Appendix B).

Working with the amplitude in Eq. (5), straightforward algebra now translates the Fig. 1–Eq. (3) Faddeev equation into a linear, homogeneous matrix equation for the coefficient functions that may figuratively be written as follows:

$$\begin{bmatrix} \mathcal{S}_\rho^P(k;Q) \\ \mathcal{A}_{\mu\rho}^{jP}(k;Q) \\ \mathcal{P}_\rho^P(k;Q) \\ \mathcal{V}_{\mu\rho}^P(k;Q) \end{bmatrix} u_\rho$$

$$= 2\int\frac{d^4\ell}{(2\pi)^4}[\mathcal{K}_{(\mu\nu)}^{(jm)}(k,\ell;Q)]\begin{bmatrix} \mathcal{S}_\rho^P(k;Q) \\ \mathcal{A}_{\nu\rho}^{mP}(k;Q) \\ \mathcal{P}_\rho^P(k;Q) \\ \mathcal{V}_{\nu\rho}^P(k;Q) \end{bmatrix} u_\rho, \tag{9}$$

in which, e.g., working from Eq. (4), the $\mathcal{A}_{\mu\rho}^j$–$\mathcal{A}_{\nu\rho}^m$ entry in the kernel matrix is

$$\mathcal{K}_{\mu\nu}^{jm}(k,\ell;Q) = \mathsf{t}^j\Gamma_\alpha^{1^+}(k_q - \ell_d/2;\ell_d)S^T(\ell_d - k_q)$$
$$\times \mathsf{t}^m\bar{\Gamma}_\mu^{1^+}(\ell_q - k_d/2;-k_d)S(\ell_q)\Delta_{\alpha\nu}^{1^+}(\ell_d), \tag{10}$$

where the isospin matrices are

$$\mathsf{t}^+ = \frac{1}{\sqrt{2}}(\tau^0 + \tau^3), \qquad \mathsf{t}^0 = \tau^1, \tag{11}$$

$\tau^0 = \mathrm{diag}[1,1]$, $\{\tau^i|i = 1, 2, 3\}$ are the usual Pauli matrices. As highlighted above, the kernel matrix draws connections between all diquark correlations in the complete amplitude, Eq. (5), e.g., $\mathcal{S} \to \mathcal{S}, \mathcal{A}, \mathcal{P}, \mathcal{V}$; and when written explicitly for all scalar functions in Eq. (6), $[\mathcal{K}_{(\mu\nu)}^{(jm)}]$ is a 28×28 matrix. This is reduced to 20×20 if one exploits isospin symmetry for the axialvector diquarks.

The diquark correlation amplitudes are explained in Ref. [34] [Eq. (1)], but it is worth repeating some of the information here:

$$\Gamma^{0^+}(k;K) = g_{0^+}i\gamma_5Ci\tau^2\vec{H}\mathcal{F}(k^2/\omega_{0^+}^2), \tag{12a}$$

$$\mathsf{t}^j\Gamma_\mu^{1^+}(k;K) = ig_{1^+}\gamma_\mu C\mathsf{t}^j\vec{H}\mathcal{F}(k^2/\omega_{1^+}^2), \tag{12b}$$

$$\Gamma^{0^-}(k;K) = g_{0^-}Ci\tau^2\vec{H}\mathcal{F}(k^2/\omega_{0^-}^2), \tag{12c}$$

$$\Gamma_\mu^{1^-}(k;K) = g_{1^-}\gamma_\mu\gamma_5Ci\tau^2\vec{H}\mathcal{F}(k^2/\omega_{1^-}^2), \tag{12d}$$

where $C = \gamma_2\gamma_4$ is the charge conjugation matrix; $\vec{H} = \{i\lambda_c^7, -i\lambda_c^5, i\lambda_c^2\}$, with $\{\lambda_c^k, k = 1, ..., 8\}$ denoting Gell-Mann matrices in color space, expresses the diquarks' color antitriplet character; and $\mathcal{F}(z) = [1 - \exp(-z)]/z$. The correlation widths in Eq. (12) are defined by the related masses ([34], Eq. (5)): $\omega_{J^P}^2 = m_{J^P}^2/2$. The amplitudes are canonically normalized ([34], Eq. (3)), which entails:

$$g_{0^+} = 14.8, \qquad g_{1^+} = 12.7, \qquad g_{0^-} = 6.59,$$
$$g_{1^-}^{I=0} = 3.27, \qquad g_{1^-}^{I=1} = 1.59. \tag{13}$$

It is the coupling-squared which appears in the Faddeev kernel, so one should expect negative-parity diquarks to play a limited role in the Faddeev amplitudes.

Using the information above, and standard diquark and quark dressed-propagators—Ref. [34] [Eq. (4) and Appendix A], the masses and Faddeev amplitudes of the ground- and first-excited state in both the positive- and negative-parity $(I, J) = (\frac{1}{2}, \frac{3}{2})$ channels can be obtained straightforwardly by solving the Faddeev equation—Fig. 1, Eq. (9)—using readily available software [65,66].

Given the importance of orbital angular momentum in the discussion of $(\frac{1}{2}, \frac{3}{2}^P)$ baryons and since it is only when working with the wave function that meaningful angular momentum decompositions become available, we record here that the (unamputated) Faddeev wave function is

recovered from the amplitude by reattaching the quark and diquark propagator legs independently and appropriately to each term in Eq. (5). Namely, one multiplies Eq. (9) from the left by

$$
S(k_q)
\begin{bmatrix}
\Delta^{0^+}(k_d) & 0 & 0 & 0 \\
0 & \Delta^{1^+}_{\mu'\mu}(k_d) & 0 & 0 \\
0 & 0 & \Delta^{0^-}(k_d) & 0 \\
0 & 0 & 0 & \Delta^{1^-}_{\mu'\mu}(k_d)
\end{bmatrix}
\tag{14}
$$

to obtain a modified equation for the following wave function:

$$
\begin{aligned}
\Psi^P(k_i, \alpha_i, \sigma_i) &= [\Gamma^{0^+}(\bar{k}; K)]^{\alpha_1 \alpha_2}_{\sigma_1 \sigma_2}[\underline{\mathcal{S}}^P_\rho(k; Q)u_\rho(Q)]^{\alpha_3}_{\sigma_3} \\
&+ [\Gamma^{1^+ j}_\mu][\underline{\mathcal{A}}^{jP}_{\mu\rho}(k; Q)u_\rho(Q)] \\
&+ [\Gamma^{0^-}][\underline{\mathcal{P}}^P_\rho(k; Q)u_\rho(Q)] \\
&+ [\Gamma^{1^-}_\mu][\mathcal{V}^P_{\mu\rho}(k; Q)u_\rho(Q)],
\end{aligned}
\tag{15}
$$

where, e.g., $\underline{\mathcal{A}}^{jP}_{\mu\rho}(k; Q) = S(k_q)\Delta^{1^+}_{\mu\nu}(k_d)\mathcal{A}^{jP}_{\nu\rho}(k; Q)$. Each of the functions here has an expansion analogous to that in Eq. (6):

$$
\underline{\mathcal{S}}^P_\rho(k; Q) = \sum_{i=1}^{2} w^i_{0^+}(k; Q)\mathcal{G}^P \mathcal{X}^i_\rho(k; Q),
\tag{16a}
$$

$$
\underline{\mathcal{A}}^{jP}_{\nu\rho}(k; Q) = \sum_{i=1}^{8} w^{ji}_{1^+}(k; Q)\mathcal{G}^P \mathcal{Y}^i_{\nu\rho}(k; Q),
\tag{16b}
$$

$$
\underline{\mathcal{P}}^P_\rho(k; Q) = \sum_{i=1}^{2} w^i_{0^-}(k; Q)\mathcal{G}^{-P} \mathcal{X}^i_\rho(k; Q),
\tag{16c}
$$

$$
\underline{\mathcal{V}}^P_{\nu\rho}(k; Q) = \sum_{i=1}^{8} w^i_{1^-}(k; Q)\mathcal{G}^{-P} \mathcal{Y}^i_{\nu\rho}(k; Q).
\tag{16d}
$$

At this point, one may make the rest-frame angular momentum associations listed in Table I.

TABLE I. Working with the wave function defined in Eq. (15), decomposed as in Eq. (16), and projected into the rest frame, one has the tabulated $J = \frac{3}{2} = L + S$ angular momentum decomposition. The last row lists the associated spectroscopic label, with the $J = \frac{3}{2}$ subscript suppressed.

L	0	1	1	2	2	3
S	$\frac{3}{2}$	$\frac{3}{2}$	$\frac{1}{2}$	$\frac{3}{2}$	$\frac{1}{2}$	$\frac{3}{2}$
Ψ^P	$w^1_{1^\pm}$	$w^2_{1^\pm}$	$w^1_{0^\pm}, w^{3,4}_{1^\pm}$	$w^5_{1^\pm}$	$w^2_{0^\pm}, w^{6,7}_\pm$	$w^8_{1^\pm}$
	^4S	^4P	^2P	^4D	^2D	^4F

III. FADDEEV EQUATION SOLUTIONS

Solving the Faddeev equation with the full amplitude in Eq. (5), one obtains the following masses (in GeV):

$$
\begin{array}{cccc}
N(1520)^{\frac{3}{2}^-} & N(1700)^{\frac{3}{2}^-} & N(1720)^{\frac{3}{2}^+} & N(1900)^{\frac{3}{2}^+} \\
1.68(8) & 1.82(9) & 1.78(8) & 2.05(7)
\end{array},
\tag{17}
$$

where the indicated uncertainties express the result of a $\pm 5\%$ change in the diquark masses, Eq. (1). As explained elsewhere [34,35,47,67,68], the kernel in Fig. 1 omits all contributions that may be linked with meson-baryon final-state interactions, i.e., the terms which transform a bare-baryon into the observed state after their inclusion, e.g., via dynamical coupled channels calculations [25–29]. The Faddeev amplitudes and masses we obtain should therefore be viewed as describing the *dressed-quark core* of the bound-state, not the completely dressed, observable object [22–24]. That explains why the masses are uniformly too large.

Herein, for comparison with experiment, following Refs. [34,47,63], we subtract the mean value of the difference between our calculated masses and the real part of the related empirical pole-positions: $\delta^{N_{3/2}}_{\text{MB}} = 0.13$ GeV. The resulting comparison is displayed in Fig. 2. The calculated level orderings and splittings match well with experiment, just as they do in analogous comparisons drawn from the results in Refs. [34,47], which are also shown. These predictions might be used to assist in refining dynamical coupled channels models by providing constraints on the size of meson-baryon final-state interactions in distinct J^P channels.

In Table II we list the mass obtained for each $(\frac{1}{2}, \frac{3}{2}^\mp)$ system when the Faddeev equation is solved by keeping only one type of diquark correlation, then two, then three, and then all. Evidently, in each case, once the axialvector and scalar diquarks are included, the mass is practically unchanged by including the other correlations. This is highlighted by Table II, which lists the change in a baryon's mass generated by the progressive inclusion of additional diquark correlations, in the order $1^+ \to 1^+, 0^+ \to 1^+, 0^+, 0^- \to 1^+, 0^+, 0^- 1^-$. A pictorial representation of these results is provided in Fig. 3.

A broadly consistent yet slightly different picture appears when one considers baryon Faddeev amplitudes. Defining

$$
n_{\mathcal{A}} = \sum_{j=+,0} \sum_{i=1}^{8} \int \frac{d^4 k}{(2\pi)^4} |v^{ji}_{1^+}(k^2, k \cdot Q)|^2,
\tag{18}
$$

with analogous expressions for $n_{\mathcal{S}}, n_{\mathcal{P}}, n_{\mathcal{V}}$, then the ratios

$$
\mathbb{F}_{\mathcal{C}} = n_{\mathcal{C}}/n_{\mathcal{T}},
\tag{19}
$$

where $\mathcal{C} = \mathcal{S}, \mathcal{A}, \mathcal{P}, \mathcal{V}$ and $n_{\mathcal{T}} = n_{\mathcal{S}} + n_{\mathcal{A}} + n_{\mathcal{P}} + n_{\mathcal{V}}$, provide an indication of the relative strength of each
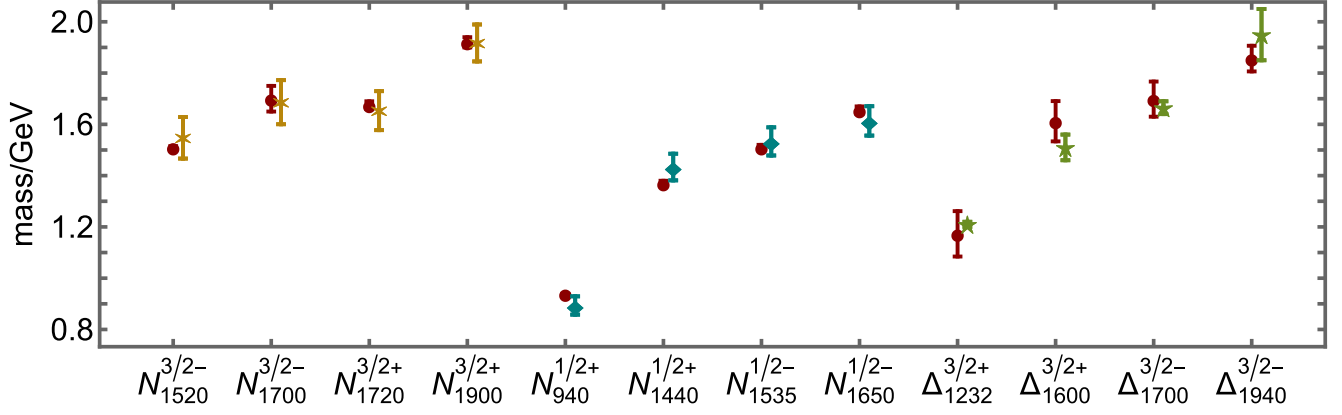
FIG. 2. Real part of empirical pole position for each identified baryon [48] (red circle) compared with: calculated masses in Eq. (17) (gold asterisks) after subtracting $\delta_{\mathrm{MB}}^{N_{3/2}} = 0.13$ GeV from each; calculated masses in Ref. [34] [Eq. (15)] (teal diamonds) after subtracting $\delta_{\mathrm{MB}}^{N_{1/2}} = 0.30$ GeV; and calculated masses in Ref. [47] (Table II) (green five-pointed stars) after subtracting $\delta_{\mathrm{MB}}^{\Delta_{3/2}} = 0.17$ GeV. All theory values are drawn with an uncertainty that reflects a $\pm 5\%$ change in diquark masses, Eq. (1).

diquark correlation in the baryon Faddeev amplitude. The calculated results are listed in Table II and drawn in Fig. 3. Axialvector diquarks dominate the Faddeev amplitude in all cases. This is partly because each baryon contains two axialvector isospin projections, whereas all other diquarks are isoscalar, and axialvector diquarks have eight distinct

contributing spinor structures. Nevertheless, channel dynamics is playing a role because the same statements are true for the proton and yet the proton amplitude is dominated by the scalar diquark ([47], Fig. 2). The scalar

TABLE II. (A) Baryon masses (in GeV) calculated using the indicated diquark correlations: all $= 1^+, 0^+, 0^-, 1^-$. (B) Change in a baryon's mass generated by the progressive inclusion of additional diquark correlations, in the order listed. (C) Fraction of a given baryon's Faddeev amplitude (FA) contributed by the different diquark correlations, defined in connection with Eq. (19). (In (B) and (C), the sum of entries in each column is unity.).

A. mass	$N(1520)\frac{3}{2}^-$	$N(1700)\frac{3}{2}^-$	$N(1720)\frac{3}{2}^+$	$N(1900)\frac{3}{2}^+$
1^+	1.84	2.06	1.90	1.98
0^+	1.99	2.22	1.98	2.15
0^-	2.34	2.59	2.49	2.61
1^-	2.49	2.72	2.44	2.62
$1^+, 0^+$	1.68	1.88	1.78	2.04
$1^+, 0^+, 0^-$	1.68	1.88	1.78	2.05
All	1.68	1.82	1.78	2.05

B. mass %	$N(1520)\frac{3}{2}^-$	$N(1700)\frac{3}{2}^-$	$N(1720)\frac{3}{2}^+$	$N(1900)\frac{3}{2}^+$
1^+	91.6	89.0	94.1	96.9
& 0^+	8.3	8.0	5.8	2.8
& 0^-	0.1	0.2	0.1	0.3
& 1^-	0.0	2.8	0.0	0.0

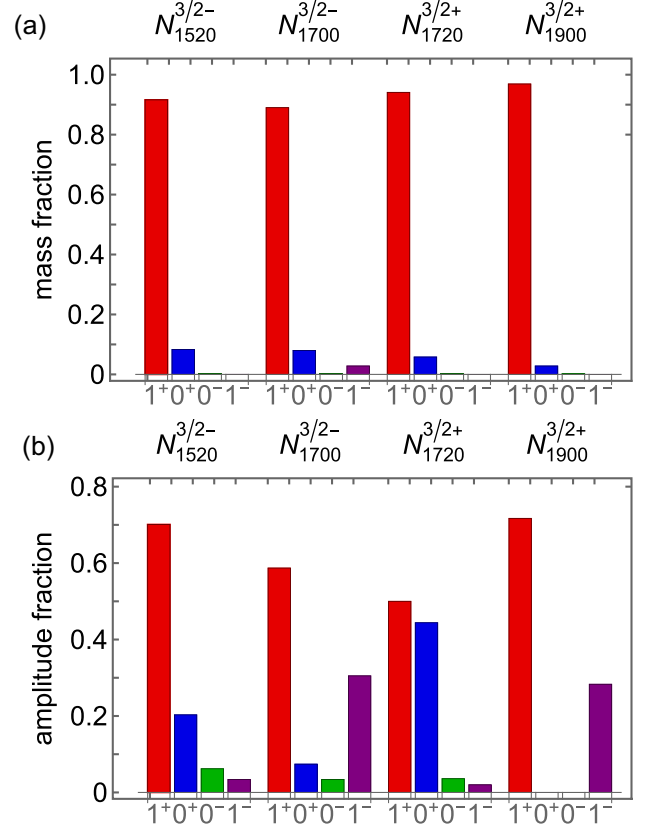| C. FA %	$N(1520)\frac{3}{2}^-$	$N(1700)\frac{3}{2}^-$	$N(1720)\frac{3}{2}^+$	$N(1900)\frac{3}{2}^+$
1^+	70.1	58.7	50.0	71.7
0^+	20.3	7.4	44.4	0.0
0^-	6.2	3.4	3.6	0.0
1^-	3.4	30.5	2.0	28.3

FIG. 3. (a) Fractional contribution to mass of $(\frac{1}{2}, \frac{3}{2}^P)$ baryons as additional diquark correlations are progressively included. (b) Fraction of a given $(\frac{1}{2}, \frac{3}{2}^P)$ baryon's Faddeev amplitude contributed by distinct diquark correlations, defined in connection with Eq. (19).

diquark is also prominent in $N(1720)\frac{3}{2}^{+}$, which is the parity partner of the $N(1520)\frac{3}{2}^{-}$; so, the differences between their amplitude fractions owe to EHM. It is interesting that the amplitudes of the other two parity partners, *viz.* $N(1700)\frac{3}{2}^{-}$, $N(1900)\frac{3}{2}^{+}$, both contain visible vector diquark fractions, when defined according to Eq. (19), and especially notable that the latter contains practically no scalar or pseudoscalar diquarks.

Such structural features can be tested in measurements of resonance electroexcitation at large momentum transfers [10,59,69,70]. In this connection, $N(1520)\frac{3}{2}^{-}$ electrocouplings are already available on the momentum transfer domain $Q_{\gamma}^2 \lesssim 5.5 m_p^2$ [59,69–73], where m_p is the proton mass. Regarding the other states mentioned here, extraction of electrocouplings on $Q_{\gamma}^2 \lesssim 5.5 m_p^2$ is underway and results are expected within two years [73]. Future experiments will collect data that can be used to determine the electrocouplings of most nucleon resonances out to $Q_{\gamma}^2 \approx 10 m_p^2$ [10,70]. This information should greatly assist in revealing measurable expressions of EHM [52–56].

IV. ORBITAL ANGULAR MOMENTUM

Given quark model expectations for $(\frac{1}{2}, \frac{3}{2}^{\mp})$ baryons, sketched in Sec. I notes (i)–(iv), it is especially interesting to consider the quark + diquark baryon rest frame orbital angular momentum, L_{qd}, decomposition obtained from their Poincaré-covariant wave functions.

One means by which to measure the strength of the various L_{qd} components is to solve the Faddeev equation for the wave function in the rest frame with first only one orbital angular momentum component and then steadily increase the L_{qd} complexity: (i) P-wave only; (ii) S-wave only; (iii) D-wave only; (iv) F-wave only; (v) P + S-wave only; etc. The results are presented in Table III and depicted in Fig. 4.

It is worth highlighting some insights revealed by Table III.

(i) For each state, a solution is obtained using only one partial wave—P, D, S, or F, and with any subset of the complete array of partial waves. Evidently, the quark-exchange kernel in Fig. 1 is very effective at binding $(\frac{1}{2}, \frac{3}{2}^{\mp})$ baryons, just as it is in every other channel considered hitherto [34,47].

(ii) Considering only single partial waves, then that which produces the lowest mass should serve as a good indicator of the dominant orbital angular momentum component in the state. This gross measure leads to the following assignments. $N(1520)\frac{3}{2}^{-}$ and $N(1700)\frac{3}{2}^{-}$ are largely P wave in character; and $N(1720)\frac{3}{2}^{+}$ and $N(1900)\frac{3}{2}^{+}$ are largely D wave states. Consequently, drawn with this broad-brush, the orbital angular momentum structure of each $(\frac{1}{2}, \frac{3}{2}^{+})$ baryon matches that which

TABLE III. (A) Calculated masses of the low-lying $(\frac{1}{2}, \frac{3}{2}^{\mp})$ baryons as obtained by stepwise including different orbital angular momentum components in the rest-frame Faddeev wave function. The italicized entries indicate the lowest mass obtained for the given state when solving with a single partial wave. (B) Change in the baryon's mass generated by progressive inclusion of additional orbital angular momentum components in its rest-frame Faddeev wave function. This information is also depicted in Fig. 4. Naturally, the sum of entries in each column is unity. (All masses in GeV.).

(A) mass	$N(1520)\frac{3}{2}^{-}$	$N(1700)\frac{3}{2}^{-}$	$N(1720)\frac{3}{2}^{+}$	$N(1900)\frac{3}{2}^{+}$
P	1.70	1.81	1.97	2.11
S	2.02	2.20	1.88	2.15
D	2.04	2.14	1.77	2.05
F	2.05	2.28	2.36	2.50
PS	1.70	1.81	2.12	2.13
PD	1.67	1.81	1.80	1.97
SD	2.14	2.18	1.77	1.89
PSD	1.68	1.81	1.80	2.05
PSDF	1.68	1.82	1.78	2.05

(B) mass %	$N(1520)\frac{3}{2}^{-}$	$N(1700)\frac{3}{2}^{-}$	$N(1720)\frac{3}{2}^{+}$	$N(1900)\frac{3}{2}^{+}$
P	98.4	99.5	1.8	3.7
S	0.1	0.4	0.2	3.6
D	1.5	0.1	97.2	92.7
F	0.0	0.0	0.8	0.0

is typical of quark models, so long as the orbital angular momentum is identified with that of a quark + diquark system.

Notwithstanding these remarks, a more complicated structural picture will be revealed below.

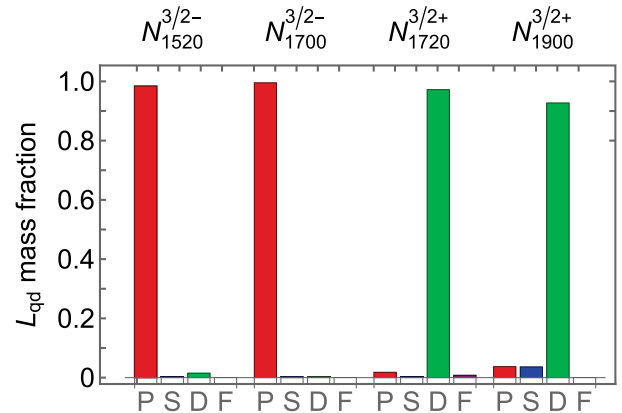The link with quark models may be augmented by considering the zeroth Chebyshev projection of the

FIG. 4. Pictorial representation of Table III. Mass fraction contribution from each rest frame partial wave in the baryon wave function, calculated as follows: $N(1520)\frac{3}{2}^{-}$, $N(1700)\frac{3}{2}^{-}$— begin with P, then add D, S, F; and $N(1900)\frac{3}{2}^{+}$, $N(1900)\frac{3}{2}^{+}$— begin with D, then add P, S, F.
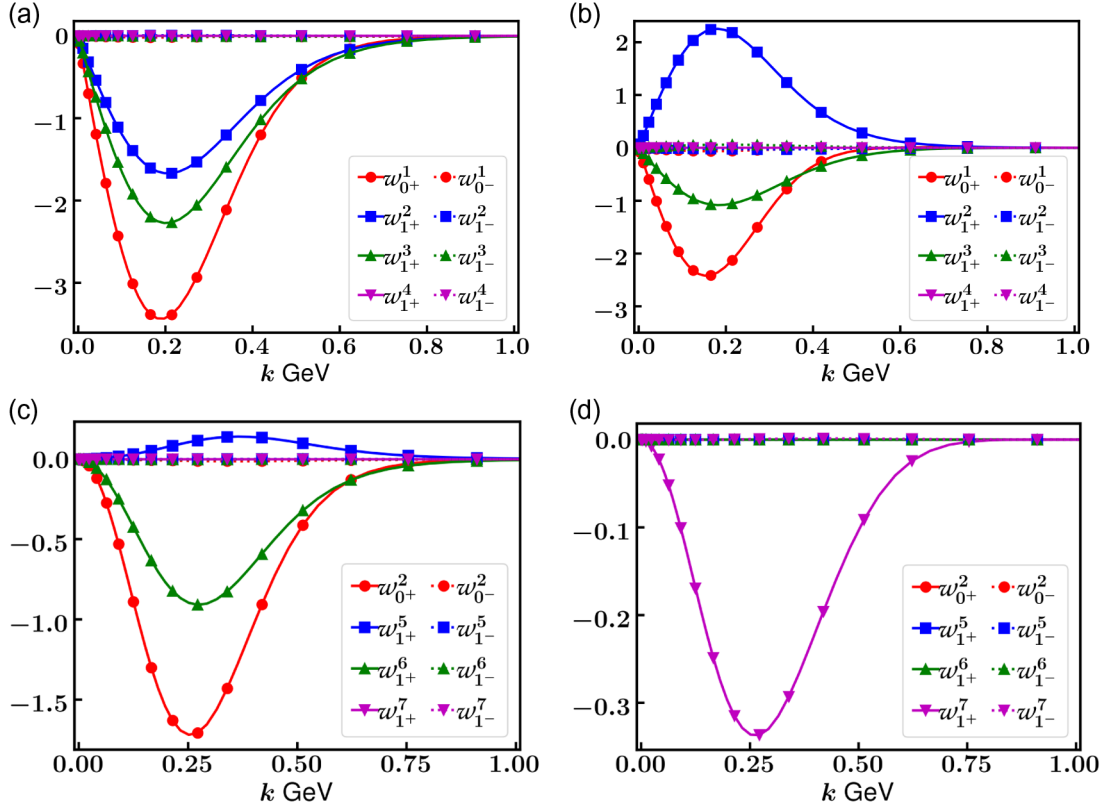
FIG. 5. Zeroth Chebyshev moments—Eq. (20). Upper panels: rest-frame P-wave components in wave functions of the negative parity baryons: (a), $N(1520)\frac{3}{2}^-$; and (b), $N(1700)\frac{3}{2}^-$. Lower panels: rest-frame D-wave components in wave functions of the positive parity baryons: (c), $N(1720)\frac{3}{2}^+$; and (d), $N(1900)\frac{3}{2}^+$.

dominant component of a baryon's Faddeev wave function,[1] as measured by the italicized entries in Table III, *viz.*

$$w^j(k^2) = \frac{2}{\pi} \int_{-1}^1 dx \sqrt{1-x^2} \, \mathsf{w}^j(k^2, x\sqrt{k^2 Q^2}), \quad (20)$$

with the terms identified using Eq. (16) and Table I of the Appendix. The results, drawn in Fig. 5, highlight that these amplitudes do not exhibit an obvious zero. Looking at the same projection of the subdominant partial waves, one finds that only a few possess such a zero. Consequently, it may reasonably be concluded that no state should be considered a radial excitation of another; hence, the collection of $(\frac{1}{2}, \frac{3}{2}^\mp)$ baryons form a set of states related via L_{qd} excitation. Such structural predictions, too, can be tested via comparisons with data obtained on the Q_γ^2-dependence of nucleon-to-resonance transition form factors [10,59,69,70].

It has often been highlighted that masses are long-wavelength observables, whose values are not very sensitive to the finer structural details expressed in a baryon's

wave function [47,53]. The apparent simplicity of the results in Fig. 4 is thus somewhat misleading. This is exposed, e.g., by performing an L_{qd} breakdown of each baryon's canonical normalization, a quantity that is related to the zero momentum transfer value of the electric form factor of the valence quarks within the state; hence, observable.[2] Those decompositions are depicted in Fig. 6, according to the assignments identified in Fig. 7, and drawn from the tables collected in the Appendix. Since negative-parity diquarks make negligible contributions to a baryon's mass—Fig. 3(a), only the scalar and axialvector contributions are recorded.

Consider first Fig. 6(a), which displays the rest-frame L_{qd}-breakdown of the $N(1520)\frac{3}{2}^-$ canonical normalization constant. Evidently, the most prominent positive contributions are provided by constructive P ⊗ D-wave interference terms; contributions from purely P-wave components

---

[1]Chebyshev polynomials of the second kind provide the natural expansion basis for a hyperspherical expansion of functions occupying a four-dimensional Euclidean space.

[2]Expressed using the wave function, the canonical normalization integrand is a sum of terms, each of which involves an inverse diquark propagator. Such functions exhibit singularities that are cancelled during integration by zeros in the wave functions. Evaluating the integrals numerically, one must use an algorithm that ensures such cancellations are perfect. No such issues arise when evaluating the normalization using the Faddeev amplitude.
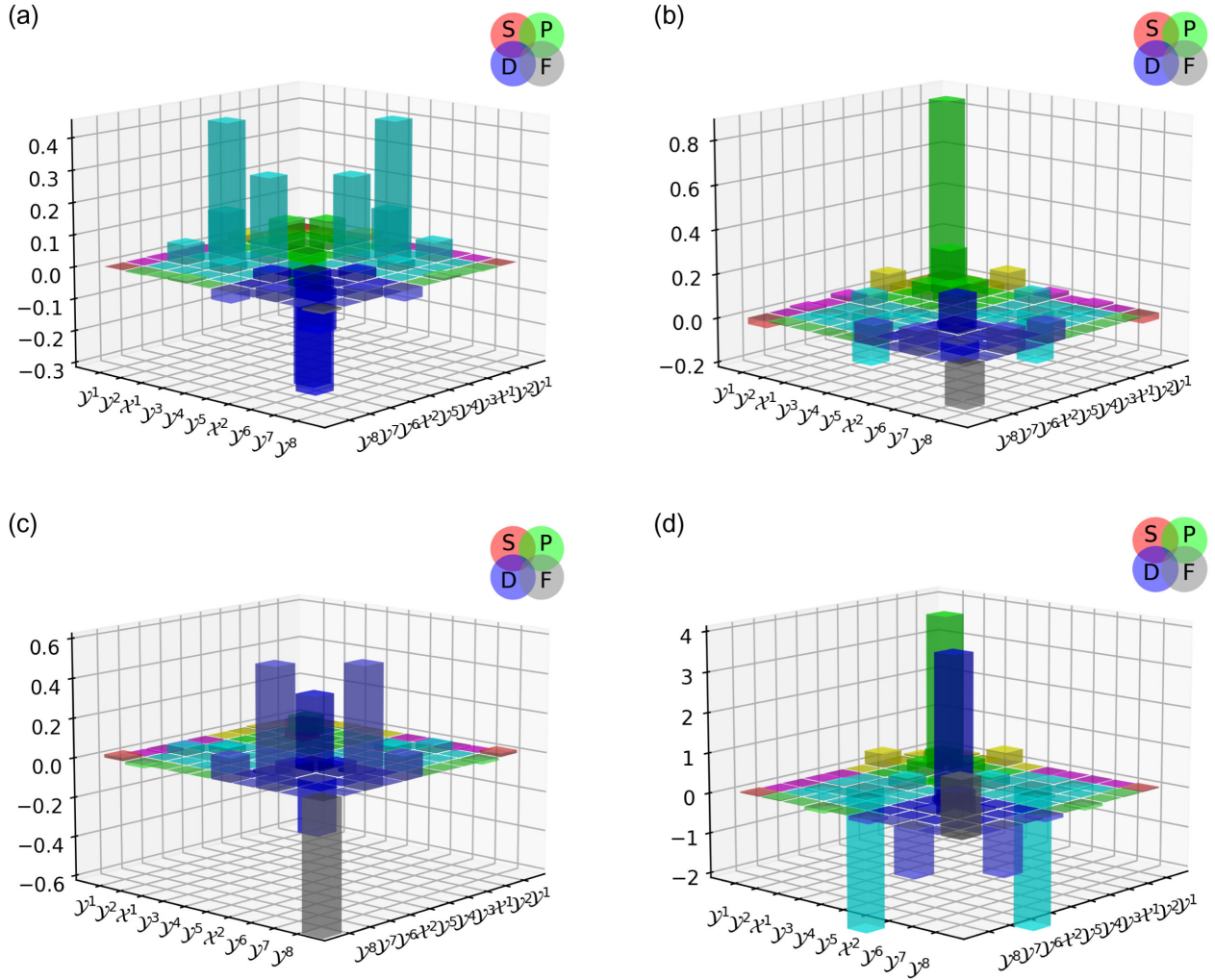
FIG. 6. Rest frame quark + diquark orbital angular momentum content of $(\frac{1}{2}, \frac{3}{2}^\mp)$ states considered herein, as measured by the contribution of the various components to the associated canonical normalization constant: (a), $N(1520)\frac{3}{2}^-$; (b), $N(1700)\frac{3}{2}^-$; (c), $N(1720)\frac{3}{2}^+$; and (d), $N(1900)\frac{3}{2}^+$. The images are drawn according to the legend in Fig. 7 and with reference to Table I, the basis in Eq. (7), and the expansion in Eq. (16). Only scalar and axialvector components are retained because they contribute most to each baryon's mass. There are both positive (above plane) and negative (below plane) contributions to the overall normalizations, which are all positive.

are visible, but interfere destructively; and pure D-wave terms are responsible for largely destructive interference. Whilst these observations are consistent with the results in Fig. 4, they also reveal the structural complexity of a Poincaré covariant wave function. This detailed picture is very different from that obtained from quark models built upon (weakly broken) SU(6) spin-flavour symmetry, as listed, e.g., in Sec. I note (i). Given that resonance electroexcitation data on this state are available out to momentum transfers $Q_\gamma^2 \approx 5.5 m_p^2$ ([59], Table IV), then our Faddeev equation structural predictions can be tested once the wave functions are used to calculate the associated transition form factors. Where such comparisons have already been made, the Faddeev equation predictions have been validated [35,36,74,75].

Turning to Fig. 6(b), the $N(1700)\frac{3}{2}^-$ wave function is seen to be less complex than that of the $N(1520)\frac{3}{2}^-$. True to Fig. 4, pure P-wave contributions to the canonical normalization are dominant; there is some destructive P ⊗ D-wave interference; simple D-wave contributions largely cancel among themselves; and D ⊗ F-wave constructive interference offsets a destructive F-wave contribution. In this case, resonance electroexcitation data is available for $Q_\gamma^2 \lesssim 1.7 m_p^2$ [76]. However, data at larger Q_γ^2 would be needed to test our structural predictions.

Drawn in Fig. 6(c), the $N(1720)\frac{3}{2}^+$ wave function is simpler still. This state is the parity partner of the $N(1520)\frac{3}{2}^-$, so differences between their wave functions are driven by EHM. Consistent with Fig. 4, normalization contributions related to D-waves are most prominent: the

FIG. 7. Legend for interpretation of Figs. 6(a)–6(d), indicating both direct terms and interference overlaps between the various identified orbital angular momentum basis components in the baryon rest frame.

largest positive terms are generated by constructive $\mathsf{D}\otimes\mathsf{F}$-wave interference. As in the $N(1700)\frac{3}{2}^-$, pure D-wave contributions largely cancel among themselves; and there is a sizeable destructive F-wave contribution. Here, too, resonance electroexcitation data is only available for $Q_\gamma^2 \lesssim 1.7 m_p^2$ [76]. Our quark + diquark Faddeev equation does not generate the $N'(1720)\frac{3}{2}^+$ state discussed in Ref. [76]. It may conceivably appear if the diquark correlations were to possess a richer structure than described by the simplified forms in Eq. (12).

The $N(1900)\frac{3}{2}^+$ normalization strengths are displayed in Fig. 6(d). This state is the parity partner of the $N(1700)\frac{3}{2}^-$. Here, EHM is seen to drive very strong pure P- and D-wave contributions. There is also a prominent constructive F-wave contribution; and $\mathsf{P}\otimes\mathsf{D}$-wave and $\mathsf{D}\otimes\mathsf{F}$-wave interference are strongly destructive. While consistent with the results drawn for this state in Fig. 4, the detailed picture is again far more complex. It is worth comparing the magnitude scale in Fig. 6(d) with that of the other panels. Owing to strong interference between partial waves, the $N(1900)\frac{3}{2}^+$ normalization constant is roughly twice that found in the other cases. This further emphasizes the complexity of its Poincaré-covariant wave function. There is currently no $N(1900)\frac{3}{2}^+$ resonance electroexcitation data ([59], Table IV).

V. SUMMARY AND PERSPECTIVE

Extending Refs. [34,47], we employed a Poincaré-covariant Faddeev equation [Fig. 1] to deliver predictions for the masses and wave functions of the four lowest lying

$(I, J^P) = (\frac{1}{2}, \frac{3}{2}^\mp)$ baryons. The Faddeev kernel is constructed using dressed-quark and nonpointlike diquark degrees-of-freedom and expresses two binding mechanisms: one is that within the diquark correlations themselves; and the other is generated by exchange of a dressed-quark, which emerges as one fully interacting diquark splits up and is subsequently absorbed into formation of another. This quark + diquark picture was introduced more than thirty years ago [30–33] and has since evolved into an efficacious tool for the prediction and explanation of baryon properties, including the large-Q_γ^2 behavior of elastic and transition form factors [39,77], axial form factors [40,43,78], and parton distribution functions [42,79],

General considerations reveal that $(\frac{1}{2}, \frac{3}{2}^\mp)$ baryons may contain five distinct types of diquark correlation: $(0,0^+)$, $(1,1^+)$, $(0,0^-)$, $(0,1^-)$, $(1,1^-)$; but our calculations showed that a good approximation is obtained by keeping only $(0,0^+)$, $(1,1^+)$ correlations [Sec. III]. This is not true for $(\frac{1}{2}, \frac{1}{2}^-)$ states, in which $(0,0^-)$, $(0,1^-)$ diquarks are important [34,45].

Exploiting our Poincaré-covariant Faddeev wave functions for $(\frac{1}{2}, \frac{3}{2}^\mp)$ baryons, we drew connections and contrasts with structural expectations deriving from quark models built upon (weakly broken) SU(6) spin-flavor symmetry [Sec. IV]. In this context, the orbital angular momentum composition was of particular interest. However, since the $J = L + S$ separation of total angular momentum into a sum of orbital angular momentum and spin is frame dependent and many quark models express only Galilean covariance, we worked with rest-frame projections of our Poincaré-covariant Faddeev wave functions. Viewed with low resolution and identifying orbital angular momentum as that which exists between dressed-quarks and -diquarks, L_{qd}, we found broad agreement. Namely, the collection of $(\frac{1}{2}, \frac{3}{2}^\mp)$ baryons form a set of states related via L_{qd} excitation: the negative parity states are primarily P-wave in nature whereas the positive parity states are D wave.

On the other hand, we also probed the structure of $(\frac{1}{2}, \frac{3}{2}^\mp)$ baryons with finer resolution, using maps of the contributions to the canonical normalization constants from the various L_{qd} components of the Poincaré-covariant wave functions. This revealed far greater complexity than typical of quark model descriptions [Fig. 6], with significant interference between L_{qd} components. These structural predictions can be tested in comparisons between measurements of resonance electroexcitation at large momentum transfers and predictions for the associated resonance electro-production form factors based on our wave functions. Concerning the $N(1520)\frac{3}{2}^-$, data already exists that could be used for this purpose and the calculations are underway. No such data exists for the other states and so our predictions are likely to encourage new experimental efforts in this area.

It is worth reiterating that the interpolating fields for negative and positive baryons are related by chiral rotation

of the quark spinors used in their construction. This entails that all differences between parity partner states owe fundamentally to chiral symmetry breaking, which is overwhelmingly dynamical in the light-quark sector [80–84]. Parity partner channels are identical when chiral symmetry is restored [85,86]. Regarding the baryons considered herein, parity connects $N(1520)\frac{3}{2}^- - N(1720)\frac{3}{2}^+$ and $N(1700)\frac{3}{2}^- - N(1900)\frac{3}{2}^+$; and we have seen that, again like the $(\frac{1}{2}, \frac{1}{2}^\pm)$ and $(\frac{3}{2}, \frac{3}{2}^\pm)$ sectors, dynamical chiral symmetry breaking (DCSB) introduces marked differences between the internal structures of parity partners. This has a marked influence on the mass splitting between the partner states and explains why it does not exhibit a simple pattern, *viz.* empirically [48]:

$$
\begin{array}{cc}
\text{states} & \text{mass splitting/GeV} \\
N(1535)\frac{1}{2}^- - N(940)\frac{1}{2}^+ & 0.57, \\
N(1650)\frac{1}{2}^- - N(1440)\frac{1}{2}^+ & 0.29, \\
\Delta(1700)\frac{3}{2}^- - \Delta(1232)\frac{3}{2}^+ & 0.46, \\
\Delta(1940)\frac{3}{2}^- - \Delta(1600)\frac{3}{2}^+ & 0.44, \\
N(1720)\frac{3}{2}^+ - N(1520)\frac{3}{2}^- & 0.17, \\
N(1900)\frac{3}{2}^+ - N(1700)\frac{3}{2}^- & 0.22.
\end{array}
\tag{21}
$$

DCSB is a corollary of emergent hadron mass (EHM); and confinement, too, may be argued to derive from EHM [54]. Thus, validating our predictions of marked structural differences between parity partners throughout the hadron spectrum has the potential to reveal much of importance about the Standard Model. As already noted, resonance electroexcitation experiments on $Q_\gamma^2 \gtrsim 2m_p^2$ are one way of achieving this goal.

Having completed this analysis, it would be natural to close the cycle and use the Poincaré-covariant quark + diquark Faddeev equation to develop structural insights into $(\frac{3}{2}, \frac{1}{2}^\pm)$ baryons. Further, in aiming to validate the pictures provided,

it is essential to calculate the electromagnetic transition form factors for all states mentioned above. Baryons containing heavier valence quarks may present additional opportunities, particularly because many models of such systems give special treatment to the heavier degrees-of-freedom, e.g., Refs. [87–92], whereas our dynamical diquark picture indicates that all valence quarks should be treated equally [63,93]. Furthermore, having highlighted the complexity of the Poincaré-covariant wave functions that describe quark-plus-dynamical-diquark systems, then our results may also have implications for studies of the tetra- and penta-quark problems, which are typically treated using very simple pictures of diquark correlations and their interactions with other bound-state constituents ([11], Sec 3.6).

APPENDIX: QUARK + DIQUARK ANGULAR MOMENTUM

Using our Faddeev equation solutions for the Poincaré-covariant baryon wave functions, evaluated in the rest frame, we computed the contributions of various quark + diquark orbital angular momentum components to each baryon's canonical normalization constant. The results are recorded in this appendix: $N(1520)\frac{3}{2}^-$: Table IV; $N(1700)\frac{3}{2}^-$: Table V; $N(1720)\frac{3}{2}^+$: Table VI; and $N(1900)\frac{3}{2}^+$: Table VII. The images in Fig. 6 are drawn from these tables.

TABLE IV. $N(1520)\frac{3}{2}^-$: quark + diquark orbital angular momentum breakdown of the canonical normalization constant, drawn in Fig. 6(a). The subarrays are composed according to the legend in Fig. 7 and the sum of all entries is unity.

	$\mathcal{Y}^1$	$\mathcal{Y}^2$	$\mathcal{X}^1$	$\mathcal{Y}^3$	$\mathcal{Y}^4$	$\mathcal{Y}^5$	$\mathcal{X}^2$	$\mathcal{Y}^6$	$\mathcal{Y}^7$	$\mathcal{Y}^8$
$\mathcal{Y}^1$	−0.01	−0.01	0.00	0.02	0.00	0.00	0.00	0.00	0.00	0.00
$\mathcal{Y}^2$	−0.01	−0.01	0.00	0.01	0.00	0.13	0.00	0.06	0.00	0.00
$\mathcal{X}^1$	0.00	0.00	−0.15	0.09	0.00	0.00	0.44	0.00	0.00	0.00
$\mathcal{Y}^3$	0.02	0.01	0.09	−0.15	0.00	0.27	0.00	0.03	0.00	0.01
$\mathcal{Y}^4$	0.00	0.00	0.00	0.00	0.00	0.00	0.00	0.00	0.00	0.00
$\mathcal{Y}^5$	0.00	0.13	0.00	0.27	0.00	−0.36	0.00	0.03	0.00	−0.03
$\mathcal{X}^2$	0.00	0.00	0.44	0.00	0.00	0.00	−0.35	0.00	0.00	0.00
$\mathcal{Y}^6$	0.00	0.06	0.00	0.03	0.00	0.03	0.00	−0.13	0.00	0.03
$\mathcal{Y}^7$	0.00	0.00	0.00	0.00	0.00	0.00	0.00	0.00	0.00	0.00
$\mathcal{Y}^8$	0.00	0.00	0.00	0.01	0.00	−0.03	0.00	0.03	0.00	−0.01

TABLE V. $N(1700)\frac{3}{2}^-$: quark + diquark orbital angular momentum breakdown of the canonical normalization constant, drawn in Fig. 6(b). The subarrays are composed according to the legend in Fig. 7 and the sum of all entries is unity.

	$\mathcal{Y}^1$	$\mathcal{Y}^2$	$\mathcal{X}^1$	$\mathcal{Y}^3$	$\mathcal{Y}^4$	$\mathcal{Y}^5$	$\mathcal{X}^2$	$\mathcal{Y}^6$	$\mathcal{Y}^7$	$\mathcal{Y}^8$
$\mathcal{Y}^1$	−0.04	−0.06	−0.04	0.08	0.00	0.02	0.00	0.01	0.00	−0.03
$\mathcal{Y}^2$	−0.06	0.87	0.00	0.00	0.00	0.05	−0.01	−0.02	0.00	0.01
$\mathcal{X}^1$	−0.04	0.00	0.21	0.08	0.00	0.00	−0.23	0.00	0.00	0.00
$\mathcal{Y}^3$	0.08	0.00	0.08	0.08	0.00	−0.02	0.00	−0.01	0.00	0.00
$\mathcal{Y}^4$	0.00	0.00	0.00	0.00	0.00	0.00	0.00	0.00	0.00	0.00
$\mathcal{Y}^5$	0.02	0.05	0.00	−0.02	0.00	−0.04	0.00	−0.01	0.00	0.09
$\mathcal{X}^2$	0.00	−0.01	−0.23	0.00	0.00	0.00	0.17	−0.01	0.00	0.00
$\mathcal{Y}^6$	0.01	−0.02	0.00	−0.01	0.00	−0.01	−0.01	−0.08	0.00	0.11
$\mathcal{Y}^7$	0.00	0.00	0.00	0.00	0.00	0.00	0.00	0.00	0.00	0.00
$\mathcal{Y}^8$	−0.03	0.01	0.00	0.00	0.00	0.09	0.00	0.11	0.00	−0.19

TABLE VI. $N(1720)\frac{3}{2}^+$: quark + diquark orbital angular momentum breakdown of the canonical normalization constant, drawn in Fig. 6(c). The subarrays are composed according to the legend in Fig. 7 and the sum of all entries is unity.

	$\mathcal{Y}^1$	$\mathcal{Y}^2$	$\mathcal{X}^1$	$\mathcal{Y}^3$	$\mathcal{Y}^4$	$\mathcal{Y}^5$	$\mathcal{X}^2$	$\mathcal{Y}^6$	$\mathcal{Y}^7$	$\mathcal{Y}^8$
$\mathcal{Y}^1$	−0.11	−0.01	0.01	0.00	0.00	0.00	0.00	−0.01	0.00	0.02
$\mathcal{Y}^2$	−0.01	0.00	0.00	0.00	0.00	−0.02	0.00	0.04	0.00	−0.01
$\mathcal{X}^1$	0.01	0.00	0.10	0.00	0.00	0.00	0.04	0.00	0.00	0.00
$\mathcal{Y}^3$	0.00	0.00	0.00	−0.01	0.00	0.00	0.00	0.01	0.00	0.00
$\mathcal{Y}^4$	0.00	0.00	0.00	0.00	0.00	0.00	0.00	0.00	0.00	0.00
$\mathcal{Y}^5$	0.00	−0.02	0.00	0.00	0.00	−0.04	0.00	−0.02	0.00	0.12
$\mathcal{X}^2$	0.00	0.00	0.04	0.00	0.00	0.00	0.37	0.06	0.00	0.00
$\mathcal{Y}^6$	−0.01	0.04	0.00	0.01	0.00	−0.02	0.06	−0.27	0.00	0.60
$\mathcal{Y}^7$	0.00	0.00	0.00	0.00	0.00	0.00	0.00	0.00	0.00	0.00
$\mathcal{Y}^8$	0.02	−0.01	0.00	0.00	0.00	0.12	0.00	0.60	0.00	−0.66

TABLE VII. $N(1900)\frac{3}{2}^+$: quark + diquark orbital angular momentum breakdown of the canonical normalization constant, drawn in Fig. 6(d). The subarrays are composed according to the legend in Fig. 7 and the sum of all entries is unity.

	$\mathcal{Y}^1$	$\mathcal{Y}^2$	$\mathcal{X}^1$	$\mathcal{Y}^3$	$\mathcal{Y}^4$	$\mathcal{Y}^5$	$\mathcal{X}^2$	$\mathcal{Y}^6$	$\mathcal{Y}^7$	$\mathcal{Y}^8$
$\mathcal{Y}^1$	−0.32	0.05	−0.04	0.35	0.00	−0.02	0.00	−0.01	0.00	0.03
$\mathcal{Y}^2$	0.05	0.27	0.00	0.00	0.00	−0.01	0.02	−0.07	0.00	0.02
$\mathcal{X}^1$	−0.04	0.00	3.95	0.34	0.00	−0.02	−3.62	−0.01	0.00	0.00
$\mathcal{Y}^3$	0.35	0.00	0.34	−0.19	0.00	0.29	−0.04	−0.09	0.00	−0.08
$\mathcal{Y}^4$	0.00	0.00	0.00	0.00	0.00	0.00	0.00	0.00	0.00	0.00
$\mathcal{Y}^5$	−0.02	−0.01	−0.02	0.29	0.00	−0.18	0.00	0.01	0.00	−0.10
$\mathcal{X}^2$	0.00	0.02	−3.62	−0.04	0.00	0.00	3.71	0.05	0.00	0.02
$\mathcal{Y}^6$	−0.01	−0.07	−0.01	−0.09	0.00	0.01	0.05	0.60	0.00	−1.18
$\mathcal{Y}^7$	0.00	0.00	0.00	0.00	0.00	0.00	0.00	0.00	0.00	0.00
$\mathcal{Y}^8$	0.03	0.02	0.00	−0.08	0.00	−0.10	0.02	−1.18	0.00	1.40

[1] S. J. Brodsky, A. Deur, and C. D. Roberts, Artificial dynamical effects in quantum field theory, Nat. Rev. Phys. **4,** 489 (2022).

[2] R. G. Edwards, J. J. Dudek, D. G. Richards, and S. J. Wallace, Excited state baryon spectroscopy from lattice QCD, Phys. Rev. D **84,** 074508 (2011).

[3] G. Eichmann, H. Sanchis-Alepuz, R. Williams, R. Alkofer, and C. S. Fischer, Baryons as relativistic three-quark bound states, Prog. Part. Nucl. Phys. **91,** 1 (2016).

[4] S.-X. Qin and C. D. Roberts, Impressions of the continuum bound state problem in QCD, Chin. Phys. Lett. **37,** 121201 (2020).

[5] C. D. Roberts, A. G. Williams, and G. Krein, On the implications of confinement, Int. J. Mod. Phys. A **07,** 5607 (1992).

[6] C. D. Roberts, Hadron properties and Dyson-Schwinger equations, Prog. Part. Nucl. Phys. **61,** 50 (2008).

[7] T. Horn and C. D. Roberts, The pion: An enigma within the standard model, J. Phys. G **43,** 073001 (2016).

[8] I. G. Aznauryan *et al.*, Studies of nucleon resonance structure in exclusive meson electroproduction, Int. J. Mod. Phys. E **22,** 1330015 (2013).

[9] W. J. Briscoe, M. Döring, H. Haberzettl, D. M. Manley, M. Naruki, I. I. Strakovsky, and E. S. Swanson, Physics opportunities with meson beams, Eur. Phys. J. A **51,** 129 (2015).

[10] S. J. Brodsky *et al.*, Strong QCD from hadron structure experiments, Int. J. Mod. Phys. E **29,** 2030006 (2020).

[11] M. Y. Barabanov *et al.*, Diquark Correlations in hadron physics: Origin, impact and evidence, Prog. Part. Nucl. Phys. **116,** 103835 (2021).

[12] H. J. Munczek, Dynamical chiral symmetry breaking, Goldstone's theorem and the consistency of the Schwinger-Dyson and Bethe-Salpeter Equations, Phys. Rev. D **52,** 4736 (1995).

[13] A. Bender, C. D. Roberts, and L. von Smekal, Goldstone theorem and diquark confinement beyond rainbow- ladder approximation, Phys. Lett. B **380,** 7 (1996).

[14] S.-X. Qin, C. D. Roberts, and S. M. Schmidt, Ward-Green-Takahashi identities and the axial-vector vertex, Phys. Lett. B **733,** 202 (2014).

[15] D. Binosi, L. Chang, S.-X. Qin, J. Papavassiliou, and C. D. Roberts, Symmetry preserving truncations of the gap and Bethe-Salpeter equations, Phys. Rev. D **93,** 096010 (2016).

[16] G. Eichmann, R. Alkofer, A. Krassnigg, and D. Nicmorus, Nucleon Mass from a Covariant Three-Quark Faddeev Equation, Phys. Rev. Lett. **104,** 201601 (2010).

[17] H. Sanchis-Alepuz, G. Eichmann, S. Villalba-Chavez, and R. Alkofer, Delta and Omega masses in a three-quark covariant Faddeev approach, Phys. Rev. D **84,** 096003 (2011).

[18] H. Sanchis-Alepuz and C. S. Fischer, Octet and Decuplet masses: A covariant three-body Faddeev calculation, Phys. Rev. D **90,** 096001 (2014).

[19] G. Eichmann, C. S. Fischer, and H. Sanchis-Alepuz, Light baryons and their excitations, Phys. Rev. D **94,** 094033 (2016).

[20] S.-X. Qin, C. D. Roberts, and S. M. Schmidt, Poincaré-covariant analysis of heavy-quark baryons, Phys. Rev. D **97,** 114017 (2018).

[21] S.-X. Qin, C. D. Roberts, and S. M. Schmidt, Spectrum of light- and heavy-baryons, Few Body Syst. **60,** 26 (2019).

[22] G. Eichmann, R. Alkofer, I. C. Cloet, A. Krassnigg, and C. D. Roberts, Perspective on rainbow-ladder truncation, Phys. Rev. C **77,** 042202(R) (2008).

[23] G. Eichmann, I. C. Cloet, R. Alkofer, A. Krassnigg, and C. D. Roberts, Toward unifying the description of meson and baryon properties, Phys. Rev. C **79,** 012202(R) (2009).

[24] H. L. L. Roberts, L. Chang, I. C. Cloet, and C. D. Roberts, Masses of ground and excited-state hadrons, Few Body Syst. **51,** 1 (2011).

[25] B. Julia-Diaz, T. S. H. Lee, A. Matsuyama, and T. Sato, Dynamical coupled-channel model of pi N scattering in the $W \le 2$-GeV nucleon resonance region, Phys. Rev. C **76,** 065201 (2007).

[26] N. Suzuki, B. Julia-Diaz, H. Kamano, T. S. H. Lee, A. Matsuyama, and T. Sato, Disentangling the Dynamical Origin of P-11 Nucleon Resonances, Phys. Rev. Lett. **104,** 042302 (2010).

[27] D. Rönchen, M. Döring, F. Huang, H. Haberzettl, J. Haidenbauer, C. Hanhart, S. Krewald, U. G. Meissner, and K. Nakayama, Coupled-channel dynamics in the reactions $\pi N \to \pi N$, ηN, $K\Lambda$, $K\Sigma$, Eur. Phys. J. A **49,** 44 (2013).

[28] H. Kamano, S. X. Nakamura, T. S. H. Lee, and T. Sato, Nucleon resonances within a dynamical coupled-channels model of πN and γN reactions, Phys. Rev. C **88,** 035209 (2013).

[29] H. García-Tecocoatzi, R. Bijker, J. Ferretti, and E. Santopinto, Self-energies of octet and decuplet baryons due to the coupling to the baryon-meson continuum, Eur. Phys. J. A **53,** 115 (2017).

[30] R. T. Cahill, C. D. Roberts, and J. Praschifka, Baryon structure and QCD, Aust. J. Phys. **42,** 129 (1989).

[31] C. J. Burden, R. T. Cahill, and J. Praschifka, Baryon structure and QCD: Nucleon calculations, Aust. J. Phys. **42,** 147 (1989).

[32] H. Reinhardt, Hadronization of quark flavor dynamics, Phys. Lett. B **244,** 316 (1990).

[33] G. V. Efimov, M. A. Ivanov, and V. E. Lyubovitskij, Quark-diquark approximation of the three quark structure of baryons in the quark confinement model, Z. Phys. C **47,** 583 (1990).

[34] C. Chen, B. El-Bennich, C. D. Roberts, S. M. Schmidt, J. Segovia, and S. Wan, Structure of the nucleon's low-lying excitations, Phys. Rev. D **97,** 034016 (2018).

[35] V. D. Burkert and C. D. Roberts, Colloquium: Roper resonance: Toward a solution to the fifty-year puzzle, Rev. Mod. Phys. **91,** 011003 (2019).

[36] C. D. Roberts, N* structure and strong QCD, Few Body Syst. **59,** 72 (2018).

[37] M. Sun *et al.*, Roper state from overlap fermions, Phys. Rev. D **101,** 054511 (2020).

[38] C. D. Roberts, R. J. Holt, and S. M. Schmidt, Nucleon spin structure at very high x, Phys. Lett. B **727,** 249 (2013).

[39] Z.-F. Cui, C. Chen, D. Binosi, F. de Soto, C. D. Roberts, J. Rodríguez-Quintero, S. M. Schmidt, and J. Segovia, Nucleon elastic form factors at accessible large spacelike momenta, Phys. Rev. D **102,** 014043 (2020).

[40] C. Chen, C. S. Fischer, C. D. Roberts, and J. Segovia, Nucleon axial-vector and pseudoscalar form factors and PCAC relations, Phys. Rev. D **105,** 094022 (2022).

[41] Z.-F. Cui, F. Gao, D. Binosi, L. Chang, C. D. Roberts, and S. M. Schmidt, Valence quark ratio in the proton, Chin. Phys. Lett. **39,** 041401 (2022).

[42] L. Chang, F. Gao, and C. D. Roberts, Parton distributions of light quarks and antiquarks in the proton, Phys. Lett. B **829,** 137078 (2022).

[43] C. Chen and C. D. Roberts, Nucleon axial form factor at large momentum transfers, Eur. Phys. J. A **58,** 206 (2022).

[44] P. Cheng, F. E. Serna, Z.-Q. Yao, C. Chen, Z.-F. Cui, and C. D. Roberts, Contact interaction analysis of octet baryon axial-vector and pseudoscalar form factors, Phys. Rev. D **106,** 054031 (2022).

[45] K. Raya, L. X. Gutiérrez-Guerrero, A. Bashir, L. Chang, Z. F. Cui, Y. Lu, C. D. Roberts, and J. Segovia, Dynamical diquarks in the $\gamma^{(*)}p \to N(1535)\frac{1}{2}^-$ transition, Eur. Phys. J. A **57,** 266 (2021).

[46] V. Crede and W. Roberts, Progress towards understanding baryon resonances, Rep. Prog. Phys. **76,** 076301 (2013).

[47] L. Liu, C. Chen, Y. Lu, C. D. Roberts, and J. Segovia, Composition of low-lying $J = \frac{3}{2}^\pm$ Δ-baryons, Phys. Rev. D **105,** 114047 (2022).

[48] R. L. Workman *et al.*, Review of particle physics, Prog. Theor. Exp. Phys. **2022,** 083C01 (2022).

[49] U. Löring, K. Kretzschmar, B. C. Metsch, and H. R. Petry, Relativistic quark models of baryons with instantaneous forces: Theoretical background, Eur. Phys. J. A **10,** 309 (2001).

[50] U. Löring, B. C. Metsch, and H. R. Petry, The light baryon spectrum in a relativistic quark model with instanton induced quark forces: The nonstrange baryon spectrum and ground states, Eur. Phys. J. A **10,** 395 (2001).

[51] S. J. Brodsky, G. F. de Teramond, H. G. Dosch, and J. Erlich, Light-front holographic QCD and emerging confinement, Phys. Rep. **584,** 1 (2015).

[52] C. D. Roberts, Empirical consequences of emergent mass, Symmetry **12,** 1468 (2020).

[53] C. D. Roberts, On mass and matter, AAPPS Bull. **31,** 6 (2021).

[54] C. D. Roberts, D. G. Richards, T. Horn, and L. Chang, Insights into the emergence of mass from studies of pion and kaon structure, Prog. Part. Nucl. Phys. **120,** 103883 (2021).

[55] D. Binosi, Emergent hadron mass in strong dynamics, Few Body Syst. **63,** 42 (2022).

[56] J. Papavassiliou, Emergence of mass in the gauge sector of QCD, Chin. Phys. C **46,** 112001 (2022).

[57] M. Ding, C. D. Roberts, and S. M. Schmidt, Emergence of hadron mass and structure, arXiv:2211.07763.

[58] C. D. Roberts, Origin of the proton mass, arXiv:2211.09905.

[59] V. I. Mokeev and D. S. Carman, Photo- and electrocouplings of nucleon resonances, Few Body Syst. **63,** 59 (2022).

[60] O. Denisov *et al.*, Letter of Intent (Draft 2.0): A New QCD facility at the M2 beam line of the CERN SPS, https://inspirehep.net/literature/1684784.

[61] K. Aoki *et al.*, Extension of the J-PARC hadron experimental facility: Third white paper, arXiv:2110.04462.

[62] I. C. Cloet, G. Eichmann, B. El-Bennich, T. Klähn, and C. D. Roberts, Survey of nucleon electromagnetic form factors, Few Body Syst. **46,** 1 (2009).

[63] P.-L. Yin, Z.-F. Cui, C. D. Roberts, and J. Segovia, Masses of positive- and negative-parity hadron ground-states,

including those with heavy quarks, Eur. Phys. J. C **81,** 327 (2021).

[64] J. Segovia, I. C. Cloet, C. D. Roberts, and S. M. Schmidt, Nucleon and Δ elastic and transition form factors, Few Body Syst. **55,** 1185 (2014).

[65] R. B. Lehoucq, D. C. Sorensen, and C. Yang, *ARPACK Users' Guide: Solution of Large-Scale Eigenvalue Problems with Implicitly Restarted Arnoldi Methods* (Society for Industrial and Applied Mathematics, Philadelphia, 1998).

[66] Y. Qiu, Sparse Eigenvalue Computation Toolkit as a Redesigned ARPACK (SPECTRA), https://spectralib.org/index.html (2021).

[67] M. B. Hecht, M. Oettel, C. D. Roberts, S. M. Schmidt, P. C. Tandy, and A. W. Thomas, Nucleon mass and pion loops, Phys. Rev. C **65,** 055204 (2002).

[68] H. Sanchis-Alepuz, C. S. Fischer, and S. Kubrak, Pion cloud effects on baryon masses, Phys. Lett. B **733,** 151 (2014).

[69] D. Carman, K. Joo, and V. Mokeev, Strong QCD insights from excited nucleon structure studies with CLAS and CLAS12, Few Body Syst. **61,** 29 (2020).

[70] V. I. Mokeev and D. S. Carman, New baryon states in exclusive meson photo-/electroproduction with CLAS, Rev. Mex. Fis. Suppl. **3,** 0308024 (2022).

[71] I. G. Aznauryan *et al.*, Electroexcitation of nucleon resonances from CLAS data on single pion electroproduction, Phys. Rev. C **80,** 055203 (2009).

[72] V. I. Mokeev *et al.*, New results from the studies of the $N(1440)1/2^+$, $N(1520)3/2^-$, and $\Delta(1620)1/2^-$ resonances in exclusive $ep \to e'p'\pi^+\pi^-$ electroproduction with the CLAS detector, Phys. Rev. C **93,** 025206 (2016).

[73] V. I. Mokeev, Two pion photo- and electroproduction with CLAS, EPJ Web Conf. **241,** 03003 (2020).

[74] Y. Lu, C. Chen, Z.-F. Cui, C. D. Roberts, S. M. Schmidt, J. Segovia, and H. S. Zong, Transition form factors: $\gamma^* + p \to \Delta(1232)$, $\Delta(1600)$, Phys. Rev. D **100,** 034001 (2019).

[75] V. I. Mokeev, Insight into EHM from results on electro-excitation of $\Delta(1600)3/2^+$ resonance, in *Proceedings of the Workshop on erceiving the Emergence of Hadron Mass through AMBER @ CERN—VII*, https://indico.cern.ch/event/1145356/contributions/4850020/ (2022).

[76] V. I. Mokeev *et al.*, Evidence for the $N'(1720)3/2^+$ nucleon resonance from combined studies of CLAS $\pi^+\pi^-p$ photo- and electroproduction data, Phys. Lett. B **805,** 135457 (2020).

[77] C. Chen, Y. Lu, D. Binosi, C. D. Roberts, J. Rodríguez-Quintero, and J. Segovia, Nucleon-to-Roper electromagnetic transition form factors at large Q^2, Phys. Rev. D **99,** 034013 (2019).

[78] C. Chen, C. S. Fischer, C. D. Roberts, and J. Segovia, Form factors of the nucleon axial current, Phys. Lett. B **815,** 136150 (2021).

[79] Y. Lu, L. Chang, K. Raya, C. D. Roberts, and J. Rodríguez-Quintero, Proton and pion distribution functions in counterpoint, Phys. Lett. B **830,** 137130 (2022).

[80] K. D. Lane, Asymptotic freedom and Goldstone realization of chiral symmetry, Phys. Rev. D **10,** 2605 (1974).

[81] H. D. Politzer, Effective quark masses in the chiral limit, Nucl. Phys. **B117,** 397 (1976).

[82] H. Pagels and S. Stokar, The pion decay constant, electromagnetic form-factor and quark electromagnetic selfenergy in QCD, Phys. Rev. D **20,** 2947 (1979).

[83] R. T. Cahill and C. D. Roberts, Soliton bag models of hadrons from QCD, Phys. Rev. D **32,** 2419 (1985).

[84] A. Bashir, L. Chang, I. C. Cloët, B. El-Bennich, Y.-X. Liu, C. D. Roberts, and P. C. Tandy, Collective perspective on advances in Dyson-Schwinger equation QCD, Commun. Theor. Phys. **58,** 79 (2012).

[85] C. D. Roberts and S. M. Schmidt, Dyson-Schwinger equations: Density, temperature and continuum strong QCD, Prog. Part. Nucl. Phys. **45,** S1 (2000).

[86] C. S. Fischer, QCD at finite temperature and chemical potential from Dyson–Schwinger equations, Prog. Part. Nucl. Phys. **105,** 1 (2019).

[87] D. Ebert, R. N. Faustov, and V. O. Galkin, Spectroscopy and Regge trajectories of heavy baryons in the relativistic quark-diquark picture, Phys. Rev. D **84,** 014025 (2011).

[88] J. Ferretti, Effective degrees of freedom in baryon and meson spectroscopy, Few Body Syst. **60,** 17 (2019).

[89] D. Ebert, R. N. Faustov, V. O. Galkin, and A. P. Martynenko, Mass spectra of doubly heavy baryons in the relativistic quark model, Phys. Rev. D **66,** 014008 (2002).

[90] J.-R. Zhang and M.-Q. Huang, Doubly heavy baryons in QCD sum rules, Phys. Rev. D **78,** 094007 (2008).

[91] H.-X. Chen, W. Chen, X. Liu, Y.-R. Liu, and S.-L. Zhu, A review of the open charm and open bottom systems, Rep. Prog. Phys. **80,** 076201 (2017).

[92] Q. Li, C.-H. Chang, S.-X. Qin, and G.-L. Wang, Mass spectra and wave functions of the doubly heavy baryons with $J^P = 1^+$ heavy diquark cores, Chin. Phys. C **44,** 013102 (2020).

[93] P.-L. Yin, C. Chen, G. Krein, C. D. Roberts, J. Segovia, and S.-S. Xu, Masses of ground-state mesons and baryons, including those with heavy quarks, Phys. Rev. D **100,** 034008 (2019).